Crystal structure and magnetic properties of hexagonal $R\mathrm{MnO_3}$ (R=Y, Lu, and Sc) and the effect of doping

T. Katsufuji,[1,2,*] M. Masaki,[3] A. Machida,[4] M. Moritomo,[5] K. Kato,[6] E. Nishibori,[7] M. Takata,[7] M. Sakata,[7] K. Ohoyama,[8] K. Kitazawa,[1,2] and H. Takagi[1]

[1]*Department of Advanced Materials Science, University of Tokyo, Tokyo 113-8656, Japan*
[2]*SORST, Japan Science and Technology Corporation, Saitama 332-0012, Japan*
[3]*Department of Applied Chemistry, University of Tokyo, Tokyo 113-8656, Japan*
[4]*Department of Crystalline Materials Science, Nagoya University, Nagoya 464-8603, Japan*
[5]*CIRSE, Nagoya University, Nagoya 464-8601, Japan*
[6]*SPring-8 and Japan Synchrotron Radiation Research Institute (JASRI), Hyogo 679-5198, Japan*
[7]*Department of Applied Physics, Nagoya University, Nagoya 464-8603, Japan*
[8]*Institute for Materials Research, Tohoku University, Sendai 980-8577, Japan*

(Received 7 February 2002; revised manuscript received 19 August 2002; published 31 October 2002)

A ferroelectricity-magnetism-coexisting system, hexagonal $R\mathrm{MnO_3}$ (R=Y, Lu, and Sc), has been investigated by synchrotron x-ray and neutron powder diffraction measurements. It is found from x-ray diffraction measurements that the ferroelectric polarization originates from the tilting of $\mathrm{MnO_5}$ polyhedra and the buckling of R layers, which persists up to 1000 K. Neutron diffraction measurements have revealed the reduction of ordered moments from the expected value, as well as strong magnetic diffuse scattering existing far above T_N, both of which are caused by geometrical frustration of the triangular lattice of Mn ions. We have also investigated the effects of Zr doping into the R site and have found that Zr doping drastically suppresses both ferroelectric distortion and magnetic ordering.

DOI: 10.1103/PhysRevB.66.134434 PACS number(s): 75.50.Ee, 77.80.−e, 61.10.Nz, 75.25.+z

I. INTRODUCTION

Hexagonal manganites $R\mathrm{MnO_3}$ (R is rare earth) are rare compounds in the sense that ferroelectricity and magnetism coexist in one compound. In these compounds, the Mn ions, each of which is surrounded by three in-plane and two apical oxygen ions (a $\mathrm{MnO_5}$ polyhedron), form a triangular-lattice layer and two adjacent layers are separated by a rare-earth layer, as shown in Fig. 1. Many studies have been done so far on both the ferroelectricity and magnetism of these compounds. As to the ferroelectricity, it is known that the triangular lattice of Mn ions has a $\sqrt{3}\times\sqrt{3}$ superstructure (a trimerization of Mn ions), and this distortion leads to the absence of centrosymmetry of the crystal (space group $P6_3cm$) and the appearance of ferroelectric polarization perpendicular to the layers (along the c axis).[1] Several reports[2,3] claim that the ferroelectric Curie temperature of hexagonal $R\mathrm{MnO_3}$ is ~900 K, but it has yet to be confirmed by diffraction measurements. In fact, there have been few studies on the temperature dependence of the crystal structure and the ferroelectric phase transition of hexagonal $R\mathrm{MnO_3}$ at high temperatures. One of the main purposes of the present study is to clarify the crystal structure and its temperature dependence, particularly at high temperatures, by synchrotron x-ray diffraction measurements.

Concerning the magnetism of hexagonal $R\mathrm{MnO_3}$, there are several neutron-scattering measurements[4–7] to investigate the magnetic ordering of Mn moments. According to those studies, the ordering pattern of the Mn moments in hexagonal $R\mathrm{MnO_3}$ is the so-called 120° structure, where the Mn moments lie within a layer and neighboring Mn moments in a layer are aligned by 120° different directions. The Néel temperature (T_N) ranges from 70 K to 130 K upon changing the rare earth R, and this is much lower than a Weiss temperature (θ), typically $|\theta|\sim 10T_\mathrm{N}$. This substantial reduction of T_N compared with $|\theta|$ is attributed to strong geometrical

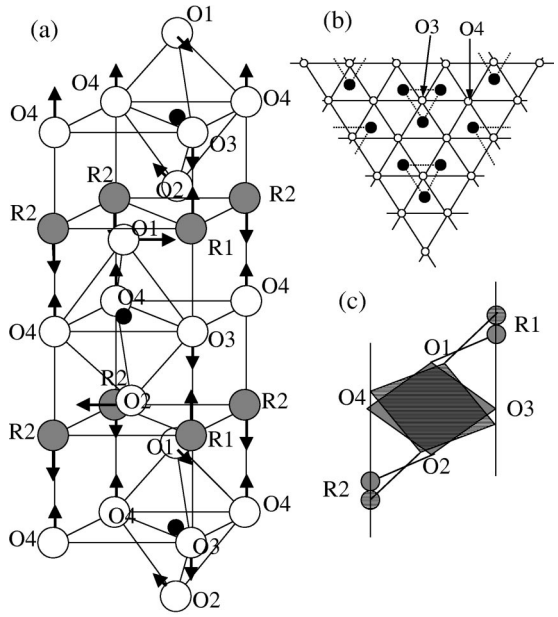

FIG. 1. (a) Schematic representation of the crystal structure of hexagonal $R\mathrm{MnO_3}$. The arrows show the displacement of each ion from the structure with a higher symmetry. (b) A structure of MnO plane, composed of Mn (solid circles) and O(3), and O(4) (open circles). The dotted lines illustrate the formation of Mn trimers. (c) A schematic picture of the tilting of a $\mathrm{MnO_5}$ polyhedron and the displacement of the rare earth.

frustration of the triangular lattice of the Mn ions.[8] We note, however, that the R dependence of the magnetic and structural properties of $R\mathrm{MnO_3}$ has not been well understood. To understand the unique coexistence of magnetism and ferroelectricity and their interplay[8–10] in hexagonal $R\mathrm{MnO_3}$, it is essential to know how various parameters, both for magnetism (Néel temperature, size of the ordered moment, etc.) and for the structure (lattice constants, lattice distortion, etc.), change under variation of R. The second purpose of this study is to clarify the R dependence of various properties in $R\mathrm{MnO_3}$, and for this purpose, we have made a systematic investigation of $R\mathrm{MnO_3}$ under variation of R, including neutron-scattering measurements to complement the studies in the past.

The third purpose is to pursue the doping effect in hexagonal $R\mathrm{MnO_3}$. It is well known that hole doping into perovskite $R\mathrm{MnO_3}$ results in the appearance of a ferromagnetic metallic phase and so-called colossal magnetoresistance.[11] As to hexagonal $R\mathrm{MnO_3}$, several reports[12–14] have been published on Ca^{2+} and Zr^{4+} doping for the R^{3+} site, as well as doping into the Mn site. However, it is not clear how such doping affects the magnetism and ferroelectricity. Here, we have tried several different types of doping and have studied the change of magnetism and structures upon doping.

II. SAMPLE PREPARATION

Single crystals of $\mathrm{YMnO_3}$ and $\mathrm{LuMnO_3}$ were grown by a floating-zone method as described in Ref. 8. A single crystal of $\mathrm{ScMnO_3}$ was not obtained by the same method. A polycrystalline sample was prepared instead following the method by Bieringer and Greedan.[6] A polycrystalline sample of $\mathrm{LuMnO_3}$ for neutron-scattering measurements was also made by a conventional solid-state-reaction method. Macroscopic properties of these samples have been published already.[8]

We tried several different types of doping into hexagonal $R\mathrm{MnO_3}$. First, Ca^{2+} doping into R^{3+}, such as $\mathrm{Lu_{1-x}Ca_x MnO_3}$, was attempted but turned out to be unsuccessful. A perovskite impurity phase was always detected, and its volume fraction estimated from the Rietveld analysis is almost the same as the concentration of doped Ca. In addition, the change of lattice constants with Ca doping was barely observed. On the other hand, Zr^{4+} doping into R^{3+} was successful. Any trace of perovskite impurity phase was not observed, and even a single crystal was grown by the floating-zone method for low Zr concentration ($\mathrm{Y_{0.95}Zr_{0.05}MnO_3}$). With increasing Zr concentration, however, a discernible amount of $\mathrm{ZrO_2}$ impurity was detected. In the case of $\mathrm{Y_{0.8}Zr_{0.2}MnO_3}$, for example, about 60% Zr precipitates as $\mathrm{ZrO_2}$ and 40% ($x=0.08$) goes into the hexagonal phase. This impurity basically does not affect the result below, except for the deviation of the composition from the nominal one. We use the nominal composition to label the samples below.

The effect of Mn-site doping was also investigated. It was found that Cr and Co doping into the Mn site always leads to perovskite impurity phases. Only Fe doping can keep the hexagonal structure up to $\sim$15% doping. However, it was found that Fe doping with this concentration least affects physical properties. Therefore, we focus only on Zr to explore the doping effect on the $R\mathrm{MnO_3}$ below.

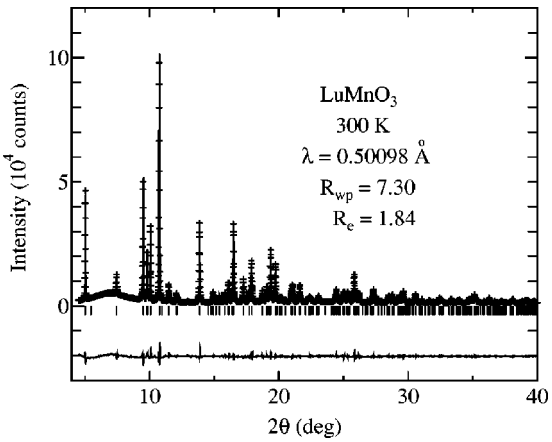

FIG. 2. Rietveld refinement patterns of the x-ray diffraction measurement for $\mathrm{LuMnO_3}$ at 300 K. Plus marks represents the observed x-ray diffraction intensities, and the solid line is calculated intensities. The vertical marks indicate the position of Bragg peaks, and the solid line at the bottom corresponds to the difference between observed and calculated intensities.

III. EXPERIMENT

A high-temperature x-ray diffraction measurement using a synchrotron radiation X-ray source was carried out at SPring-8 BL02B2 equipped with a large Debye-Sherrer camera. For the measurements, single crystals or polycrystalline samples were crushed into powder, and then a precipitation method[15] was applied to get fine powder with a homogeneous size. The powder was sealed in a 0.2- or 0.3-mm -diam quartz capillary, and temperature was controlled by a high-temperature (300–1000 K) N_2 gas flow system. The wavelength was 0.750 86 Å for the samples containing Y to avoid x-ray absorption and 0.50098 Å for the rest. One set of data was collected for 15 min.

Neutron powder diffraction measurements were performed using the Kinken powder diffractomater for high-efficiency and high-resolution measurements (HERMES) installed at the JRR-3M reactor at the Japan Atomic Energy Research Institute, Tokai, Japan.[16] Neutrons with wavelength 1.8196 Å were obtained by the 331 reflection of the Ge monochromator and 12′-B-sample-22′ collimation. About 10 g powder was sealed in a 10-mm-diam vanadium cell, and temperature control was made by a closed-cycle He-gas refrigirator between 10 and 300 K. One data point was collected for 18 min.

The obtained x-ray and neutron powder diffraction patterns were analyzed using the RIETAN-97 program to obtain structural parameters. The estimation of the size of magnetic moment with a noncollinear order was made separately by peak fitting and calculation.

IV. X-RAY DIFFRACTION MEASUREMENT

Figure 2 shows the Rietveld analysis of the x-ray diffraction pattern for $\mathrm{LuMnO_3}$ at 300 K as a typical example. First,

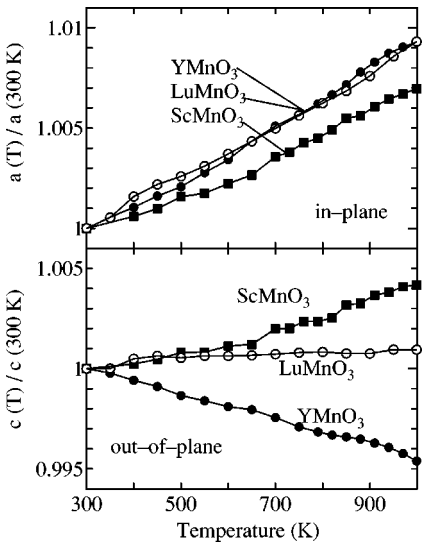

FIG. 3. Temperature dependence of the in-plane lattice constant (a) and out-of-plane lattice constant (c), both of which are normalized to the values at 300 K, for $YMnO_3$ (solid circles), $LuMnO_3$ (open circles), and $ScMnO_3$ (solid squares).

let us focus on the temperature dependence of lattice constants. As can be seen in Fig. 3, the in-plane lattice constant (a) shows a gradual increase with increasing temperature between 300 and 1000 K for all $YMnO_3$, $LuMnO_3$, and $ScMnO_3$, and this result can be explained by a simple thermal expansion. On the other hand, the lattice constant along the c axis (c) shows different behaviors depending on R. The c lattice constant increases with increasing temperature for $ScMnO_3$, whereas it rather decreases with increasing temperature for $YMnO_3$. In particular, the decrease of a lattice constant with increasing temperature (negative thermal coefficient) in $YMnO_3$ for a wide temperature range (300–1000 K) is fairly anomalous and is related to the ferroelectric distortion, as will be discussed later.

There are several reports claiming that the ferroelectric Curie temperature T_C of hexagonal $RMnO_3$ is $\sim$900 K.[2] However, we could find no evidence of a structural phase transition up to 1000 K for either $RMnO_3$ in our experiment. As an example, the x-ray diffraction patterns of $YMnO_3$ at 300 K and 1000 K are shown in Fig. 4. The peaks given by arrows correspond to those arising from the the $\sqrt{3}\times\sqrt{3}$ distortion, but they persist even up to 1000.[17] We note that lattice constants (Fig. 3) and resistivity[8] vary smoothly with temperature with no anomaly up to 1000 K. These results indicate that the ferroelectric Curie temperature is above 1000 K for any $RMnO_3$. The atomic parameters of $LuMnO_3$ and $YMnO_3$ at 300 K and 1000 K are summarized in Table I. The values of selected bond lengths are shown in Table II.

The $\sqrt{3}\times\sqrt{3}$ distortion contains the displacement of various atoms. The arrows in Fig. 1(a) illustrate the displacement of each atom from the position in the high-symmetry phase. The distortion can be roughly understood as the combination of (1) the tilting of the MnO_5 polyhedra toward O(3) (a center of the threefold symmetry) and (2) the buckling of the R plane. The Mn ions do not show any significant shift toward the center of a trimer [O(3)], indicating that the main

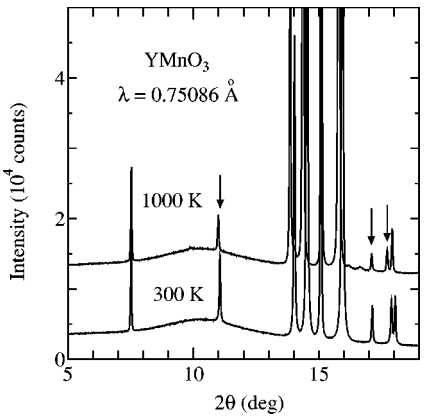

FIG. 4. X-ray diffraction patterns for $YMnO_3$ at 300 K and 1000 K. The arrows show the peaks arising from the trimer distortion.

origin of the $\sqrt{3}\times\sqrt{3}$ distortion is not the contraction of three Mn ions. It is notable that the displacement of the in-plane oxygen [O(3) and O(4)] along the c axis is opposing that of R, resulting in two R-O bonds (parallel to the c axis) with largely different lengths. Such a shift of R against the in-plane oxygen is caused by the displacement of the apical oxygen [O(1) and O(2)] along the ab plane, which pushes off R as illustrated in Fig. 1(c).

Since the R atom is off the center of two in-plane oxygen atoms along the c axis, a dipole moment exists in one O-R-O-R . . . chain in the c direction. The direction of this dipole moment is opposite between the O(4)-R(2)-O(4)-R(2) . . . chain and O(3)-R(1)-O(3)-R(1) . . . chain, but is not canceled because the number of the O(4)-R(2)-O(4)-R(2) . . . chain is twice that of the O(3)-R(1)-O(3)-R1 . . . chain. Therefore, the tilting of the MnO_5 polyhedra and the buckling of the R plane produces a *ferrielectric* state on the triangular lattice.

Another important consequence of the tilting of the MnO_5 polyhedra and the buckling of the R plane is the elongation of the c axis, as illustrated in Fig. 1(c). This counterintuitive characteristic can cause a decrease of the c lattice constant when the tilting and buckling are reduced, for example, with increasing temperature. Figure 5 shows how the magnitude of the tilting and buckling changes with temperature. Here, the magnitude of the tilting of MnO_5 polyhedra is represented by the angle between the O(3)-O(4) (in-plane oxygen) bond and the ab plane [Fig. 5(a)] and also by the angle between the O(1)-O(2) (apical oxygen) bond and the c axis [Fig. 5(b)]. The buckling of the R plane is represented by the difference of the z position of two inequivalent R ions, $R(1)z-R(2)z$ [Fig. 5(c)]. As can be seen, the magnitude of the tilting and the buckling is reduced with increasing temperature, most prominently in $YMnO_3$. Since this tilting and buckling are supposed to disappear at the ferroelectric Curie temperature T_C, the experimental result implies that $YMnO_3$ has the lowest T_C. Thus, it can be concluded that the decrease of the c lattice constant of $YMnO_3$ shown in Fig. 3 comes from the reduction of the tilting and buckling with increasing temperature, which is the largest for $YMnO_3$ among three rare earths.

TABLE I. Atomic parameters for selected RMnO$_3$ from synchrotron x-ray powder diffraction refinements. The space group is $P6_3cm$. Atomic positions: $R(1)$ at $2a$ (0,0,z), $R(2)$ at $4b$ (1/3,2/3,z), Mn at $6c$ (x,0,0), O(1) and O(2) at $6c$ (x,0,z), O(3) at $2a$ (0,0,z), and O(4) at $4b$ (1/3,2/3,z).

	Lu		Y		$Y_{0.8}Zr_{0.2}$
	300 K	1000 K	300 K	1000 K	300 K
a (Å)	6.0459(2)	6.1022(2)	6.1483(3)	6.2055(2)	6.1258(5)
c (Å)	11.4074(3)	11.4182(3)	11.4432(4)	11.3935(3)	11.2407(6)
R(1)z	0.280(2)	0.270(1)	0.2689(6)	0.2609(9)	0.251(1)
R(2)z	0.237(2)	0.234(2)	0.2294(6)	0.2328(9)	0.233(1)
Mnx	0.339(2)	0.355(1)	0.323(1)	0.326(2)	0.328(3)
O(1)x	0.319(8)	0.323(6)	0.325(2)	0.323(4)	0.331(8)
O(1)z	0.174(3)	0.161(6)	0.163(2)	0.170(3)	0.176(3)
O(2)x	0.638(6)	0.652(6)	0.629(2)	0.644(4)	0.658 (8)
O(2)z	0.344(3)	0.326(6)	0.338(2)	0.344(2)	0.344(3)
O(3)z	0.474(5)	0.467(5)	0.484(3)	0.487(3)	0.509(3)
O(4)z	0.022(3)	0.011(4)	0.022(2)	0.020(2)	0.029(2)

Zr doping has a conspicuous effect on the crystal structure of RMnO$_3$. As shown in Table I, the c lattice constant is substantially ($\sim$2%) decreased with Zr doping. As discussed above, the shorter c axis implies a smaller magnitude of the tilting of MnO$_5$ and the buckling of the R plane. Such a reduction of the distortion is experimentally seen in the x-ray diffraction pattern, as shown in Fig. 6, where the peaks arising from the $\sqrt{3}\times\sqrt{3}$ distortion drastically decrease in their intensity with Zr doping. The magnitude of the tilting and the buckling obtained from Rietveld analysis is shown in Fig. 7. These results indicate that Zr doping heavily reduces the ferroelectric distortion of RMnO$_3$. The origin of this doping effect will be discussed in Sec. VI.

V. NEUTRON-SCATTERING MEASUREMENT

In neutron diffraction patterns of LuMnO$_3$, magnetic Bragg peaks grow below $T_N=86$ K, as shown in Fig. 8(a). It is known that, although all RMnO$_3$ has magnetic ordering with 120° structure, there remain two degrees of freedom, the direction of the magnetic moment (represented by φ) and the relation between two adjacent MnO layers (''parallel'' or ''antiparallel''), as illustrated in Fig. 9(a). We note that the (100) peak, which should appear at $\sim$20°, is almost absent in LuMnO$_3$. If there is no $\sqrt{3}\times\sqrt{3}$ distortion, this peak is forbidden when the spin configuration is (1) ''parallel'' and $\varphi=90°$ [Fig. 9(b)] or (2) ''antiparallel'' and $\varphi=0°$ [Fig. 9(c)]. In fact, these two spin configurations produce completely the same peak profile if there is no distortion. Though it is in principle possible to discriminate these two spin configurations in the presence of the $\sqrt{3}\times\sqrt{3}$ distortion, our experimental accuracy is not enough to identify the correct spin configuration. From nonlinear optical measurements, Fiebig *et al.*[21] reported that parallel and $\varphi=90°$ is the correct spin configuration of LuMnO$_3$.[22]

TABLE II. Values of selected bond lengths from synchrotron x-ray powder diffraction refinements for ScMnO$_3$, LuMnO$_3$, and YMnO$_3$, at 300 K and 1000 K, respectively. The bonds in parentheses are for the average values.

	ScMnO$_3$		LuMnO$_3$		YMnO$_3$	
	300 K	1000 K	300 K	1000 K	300 K	1000 K
Mn-O(1)	1.92(2)	1.93(3)	1.98(3)	1.85(7)	1.86(2)	1.94(3)
Mn-O(2)	1.84(2)	1.85(3)	1.78(3)	1.98(6)	1.87(2)	1.79(3)
Mn-O(3)	2.01(1)	2.065(9)	2.07(2)	2.20(1)	1.999(7)	2.03(1)
Mn-O(4)	1.944(5)	1.950(6)	2.013(8)	1.974(5)	2.096(4)	2.104(6)
(Mn-O)	1.93	1.95	1.97	2.00	1.98	1.99
$R(1)$-O(1)	2.30(2)	2.33(3)	2.28(4)	2.33(5)	2.34(2)	2.26(3)
$R(1)$-O(2)	2.29(1)	2.21(3)	2.31(4)	2.22(4)	2.42(2)	2.41(3)
$R(1)$-O(3)	2.20(4)	2.02(4)	2.21(5)	2.25(6)	2.46(3)	2.57(3)
[$R(1)$-O]	2.28	2.23	2.28	2.27	2.39	2.37
$R(2)$-O(1)	2.05(1)	2.15(2)	2.18(3)	2.23(3)	2.21(1)	2.22(1)
$R(2)$-O(2)	2.16(1)	2.11(2)	2.29(2)	2.25(4)	2.31(1)	2.37(1)
$R(2)$-O(4)	2.33(2)	2.46(2)	2.46(3)	2.54(4)	2.37(2)	2.42(2)
[$R(2)$-O]	2.14	2.18	2.27	2.28	2.28	2.31
(R-O)	2.19	2.20	2.27	2.28	2.32	2.33

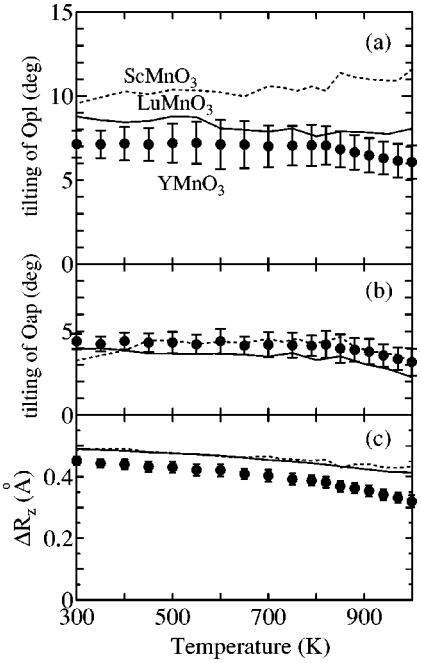

FIG. 5. Temperature dependence of (a) the tilting angle of in-plane oxygen ions, (b) the tilting angle of apical oxygen ions, and (c) the magnitude of the buckling of *R* ions. Solid circles with error bars, solid lines, and dotted lines are the data of $YMnO_3$, $LuMnO_3$, and $ScMnO_3$, respectively. The error bars for $LuMnO_3$ and $ScMnO_3$ are omitted for clarity of the figure, but are comparable with those of $YMnO_3$.

Figure 10 plots the temperature dependence of the size of magnetic moment.[18] The magnetic moment at 10 K is $\sim 3.1\mu_B$, which is discernibly smaller than the expected value for Mn^{3+} ($S=2$), $4\mu_B$. Such reduction of the magnetic moment is also observed in $YMnO_3$ ($2.90\mu_B$) and $ScMnO_3$ ($3.54\mu_B$) in a previous study.[7]

Another feature related to magnetism is a broad peak around the (100) peak ($\sim 20°$, forbidden in $LuMnO_3$), most strongly observed around T_N as shown in Fig. 11, which can be assigned to a magnetic diffuse scattering.[6] What is striking in $LuMnO_3$ is that this magnetic diffuse scattering sur-

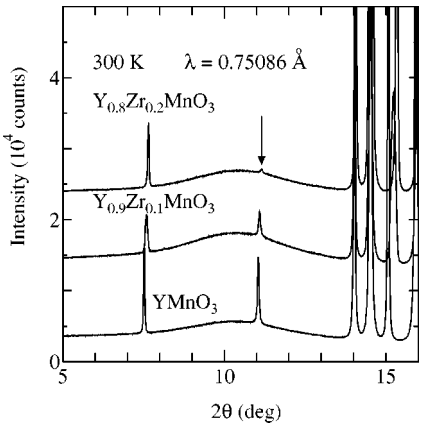

FIG. 6. X-ray diffraction patterns of $Y_{1-x}Zr_xMnO_3$. The arrow shows the peaks arising from the trimer distorion.

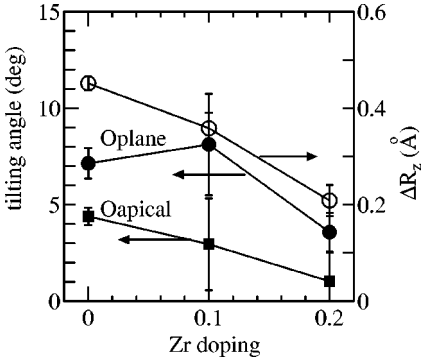

FIG. 7. The tilting angle of in-plane oxygen ions (solid circles, the left axis) and apical oxygen ions (solid squares, the left axis), and the magnitude of the *R* buckling (open circles, the right axis) as a function of Zr concentration for $Y_{1-x}Zr_xMnO_3$.

vives at least up to 220 K ($\sim 3T_N$). This result indicates that a spin fluctuation exists far above T_N in $LuMnO_3$. As discussed in Sec. I, the Weiss temperature ($|\theta|$) of $RMnO_3$ is much higher than T_N (typically $\sim 10T_N$), and such a suppression of T_N compared with $|\theta|$ is attributed to the strong geometrical frustration inherent to the triangular lattice. We note that magnetic diffuse scattering far above the ordering temperature has been observed in many spin systems with strong geometrical frustration and is attributed to quantum critical fluctuations of antiferromagnetic spin clusters for $T_N < T \ll |\theta|$.[23,24] Thus, it can be speculated that the observed magnetic diffuse scattering in hexagonal $RMnO_3$ has the same origin. To further investigate this magnetic diffuse scattering, a study of the energy dependence, i.e., a neutron-inelastic-scattering measurements is necessary.

Zr doping affects also the magnetic ordering. As shown in Fig. 8(b), the intensity of the magnetic Bragg peaks is heavily suppressed for $Lu_{0.8}Zr_{0.2}MnO_3$.[25] On the other hand, the magnetic diffuse scattering, which disappears at the low-

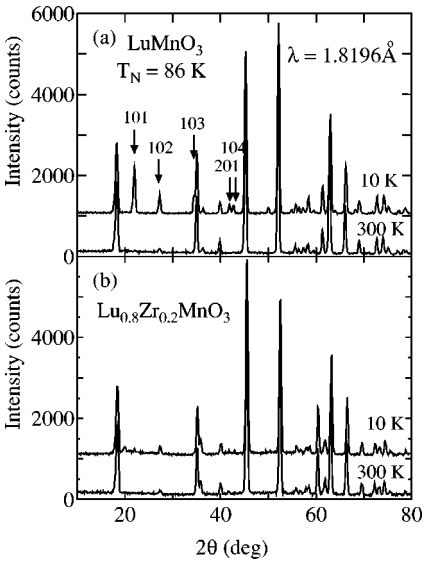

FIG. 8. Neutron diffraction patterns of (a) $LuMnO_3$ and (b) $Lu_{0.8}Zr_{0.2}MnO_3$ at 100 K and 300 K. The arrows with Miller indices refer to magnetic Bragg peaks.

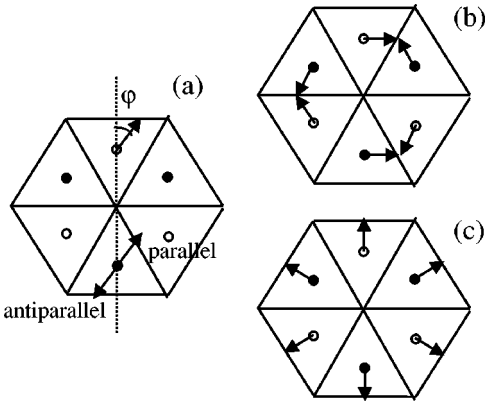

FIG. 9. (a) A schematic picture of spin ordering with the angle ψ in the parallel and antiparallel configurations. Open circles indicate Mn ions in a layer, and solid circles indicate Mn ions in the next layer separated by $z/2$. (b) and (c) illustrate two possible spin configurations for $LuMnO_3$.

est temperature for pure $LuMnO_3$, exists even at the lowest temperature for the Zr-doped sample, as shown in Fig. 12. This clearly indicates that Zr doping changes the long-range ordering of the Mn moments into short-range antiferromagnetic clusters even at the lowest temperature. This result will be discussed in the next section.

VI. DISCUSSION

The R dependences of several important parameters are summerized in Fig. 13, where the x axis denotes the ionic radius of R. Lattice constants a and c are plotted in Fig. 13(a), which increase with increasing the ionic radius of R. Figure 13(b) plots the thermal expansion coefficients $(\Delta a/\Delta T)/a$ and $(\Delta c/\Delta T)/c$, which are determined by fitting the data of the lattice constant vs temperature to a linear function between 300 and 700 K. The behavior of $(\Delta c/\Delta T)/c$ has been discussed in Sec. IV. The tilting angle of MnO_5 polyhedra increases with decreasing the ionic radius of R [Fig. 13(c)]. A similar relation has been observed in perovskite structures AMO_3 with so-called $GdFeO_3$ distortion, where the tilting angle of MO_6 octahedra increases with

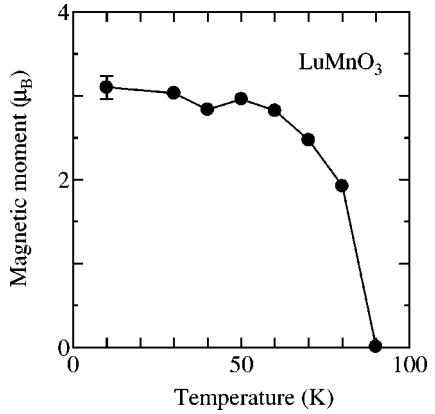

FIG. 10. Temperature vs magnetic moment for $LuMnO_3$ estimated from neutron diffraction measurements.

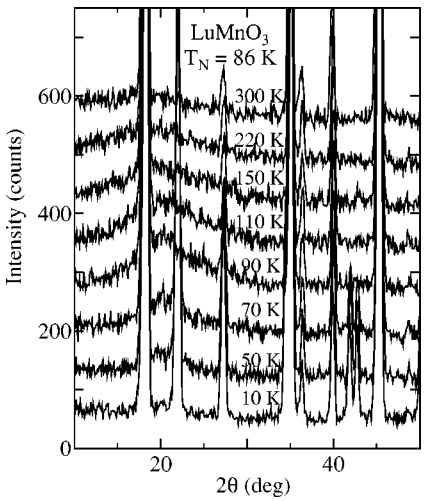

FIG. 11. Neutron diffraction patterns expanded along the y axis for $LuMnO_3$ at various temperatures. Broad peaks corresponds to magnetic diffuse scattering.

decreasing the ionic radius of A.[26] This tilting of MO_6 octahedra in the perovskite structure can be explained by a mismatch of the ionic radius in the crystal. That is, the ionic radius of A is too small to form a cubic perovskite structure, and thus the crystal is distorted to fill up the space around the A ions. We speculate that the tilting of $RMnO_3$ can be explained by a similar ionic model. The only difference of $RMnO_3$ from such a conventional tilting-type distortion is that the local electric polarization produced by the tilting is not canceled in the total crystal because of the triangular lattice, i.e., the odd number of MnO_5 octahedra in a unit, resulting in the remnant ferroelectric polarization.

A Néel temperature and a Weiss temperature also change with R [Fig. 13(d)], which can be explained by the change of lattice constants. Namely, as the in-plane lattice constant becomes smaller and the Mn-Mn distance becomes shorter, the exchange interaction increases and thus both the Néel temperature and Weiss temperature increase. On the other hand, the reduction of ordered magnetic moment from the expected

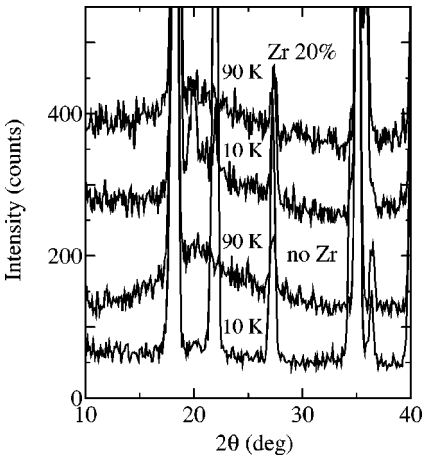

FIG. 12. Neutron diffraction patterns expanded along the y axis for $Lu_{0.8}Zr_{0.2}MnO_3$ (upper) and for $LuMnO_3$ (lower) at 90 K and 10 K.

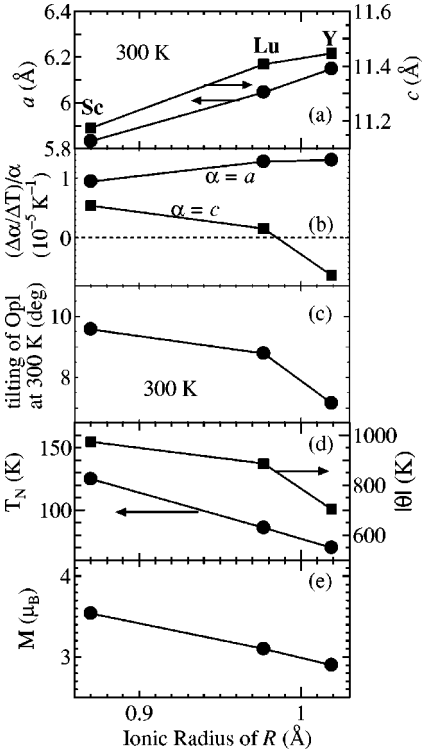

FIG. 13. (a) Lattice constants, (b) thermal expansion coefficients, (c) tilting angle of in-plane oxygen ions at 300 K, (d) Néel temperatures (left axis) and Weiss temperatures (right axis), and (e) the size of magnetic moment at the lowest temperature, as a function the ionic radius of *R*. The size of the magnetic moment for $YMnO_3$ and $ScMnO_3$ is from Ref. 7.

value ($4\mu_B$) and its *R* dependence [Fig. 13(e)] may allow several explanations. One possibility is that a part of the magnetic moment is still fluctuating even at the lowest temperature because of strong frustration of the triangular lattice. In this case, the tilting of MnO_5 polyhedra and the formation of trimers, whose magnitude increases with decreasing the ionic radius of *R*, stabilize a specific 120° structure and thus reduce the frustration, leading to a recovery of the ordered moment.

Let us move on to the effect of Zr doping. The principal effect of Zr^{4+} doping into the R^{3+} site would be electron doping into the Mn^{3+} ions, i.e., the formation of Mn^{2+}. However, experimentally confirmation of the existence of Mn^{2+} has yet to be made.[20] Here, we assume that Mn^{2+} ions exist in Zr-doped samples and continue the discussion. We note that the resistivity of Zr-doped samples is as high as that of the parent compounds $RMnO_3$,[19] indicating that Mn^{2+} is fairly localized in $R_{1-x}Zr_xMnO_3$. It is expected that the magnetic interaction between Mn^{2+}-Mn^{3+} is different from the interaction between Mn^{3+}-Mn^{3+}. In fact, the magnetic susceptibility of $YMnO_3$ is enhanced with Zr doping particularly at low temperatures, as shown in Fig. 14, indicating a drastic decrease of the Weiss temperature $|\theta|$ with a small amount of electron doping. This suggests that the Mn^{2+}-Mn^{3+} interaction is ferromagnetic and cancels the strong antiferromagnetic interaction between Mn^{3+}-Mn^{3+}. Therefore, suppression of the ordered moment and the existence of magnetic diffuse scattering at low temperatures for a Zr-doped sample can be ascribed to a spin-glass-like behavior caused by the coexistence of antiferromagnetic and ferromagnetic interactions. It should also be pointed out that a cusp of the magnetic susceptibility at T_N observed in pure $RMnO_3$ disappears with Zr doping, consistent with the suppression of the magnetic Bragg peak in neutron scattering.

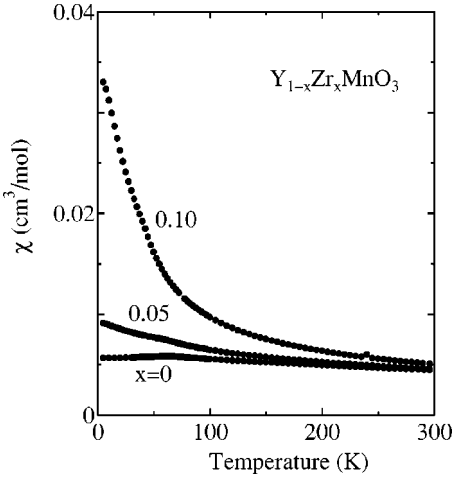

FIG. 14. Temperature dependence of the magnetic susceptibility for $Y_{1-x}Zr_xMnO_3$. Applied magnetic field is 1000 Oe.

Concerning the reduction of the tilting angle of MnO_5 polyhedra with Zr doping, several explanations are possible. On the basis of the ionic model discussed above, the change of the tilting angle with Zr doping can be attributed to the larger Mn^{2+} ion than the Mn^{3+} ion. It is not obvious, however, why a larger ionic radius on the Mn site leads to a smaller tilting angle in this structure. Another possibility is to take account of the Coulombic potential (Madelung potential), which stabilizes a specific distortion. Since Zr doping changes the amount of charge on each ion, the Madelung potential also changes, resulting in a possible change of the tilting angle. The third possibility is to take account of the hybridization between Mn $3d$ states and oxygen $2p$ states. The Mn^{3+} state in hexagonal $RMnO_3$ has an unoccupied nondegenerate $3z^2-r^2$ state, which splits from other states by $\sim$1.6 eV,[27] and this empty $3z^2-r^2$ state is occupied by one electron in Mn^{2+}. Recently, Khomskii[28] proposed that strong hybridization between occupied $2p$ states of oxygen and empty $3d$ states of transition metal is important for the ferroelectric distortion of many oxides such as $BaTiO_3$, and that explains why the coexistence of magnetism, which requires partially occupied $3d$ states, and ferroelectricity is rare. On the basis of this scenario, the empty $3z^2-r^2$ state is important for the ferroelectric distortion of $RMnO_3$, but electron doping into this $3z^2-r^2$ state by Zr doping can reduce this distortion. Further studies are required, however, to understand the reduction of ferroelectric distortion with Zr doping, which must be closely related to the origin of ferroelectricity in $RMnO_3$.

VII. SUMMARY

By synchrotron x-ray and neutron powder diffraction measurements, we have investigated hexagonal $RMnO_3$,

where ferroelectric polarization perpendicular to the Mn triangular lattice and magnetic ordering of the Mn moments with the 120° structure coexist. From synchrotron x-ray powder diffraction measurements, it is found that the electric polarization originates from the tilting of MnO_5 polyhedra and the buckling of *R* planes, which persists at least up to 1000 K. As a consequence of this distortion, lager tilting of MnO_5 causes a longer *c* axis, resulting in negative thermal coefficient of the *c* lattice constant for $YMnO_3$. Neutron diffraction measurements revealed that the size of the ordered moment is reduced from the expected value of Mn^{3+} and that magnetic diffuse scattering, indicative of spin fluctuation, exists far above T_N ($\sim 3T_N$). These magnetic properties are caused by strong geometrical frustration of spins on the triangular lattice of Mn ions. The effects of Zr doping into the *R* site (electron doping into the Mn site) were also investigated. The ferroelectric distortion, i.e., the tilting of MnO_5 polyhedra and the buckling of *R* planes, is heavily suppressed with Zr doping. The ordered magnetic moment is also suppressed but the magnetic diffuse scattering is enhanced instead with Zr doping, indicating the formation of short-range antiferromagnetic clusters at the lowest temperature. Finally, strong correlations between magnetism (Néel temperature, size of magnetic moment) and structures (lattice constants, lattice distortion) have been demonstrated from the *R* dependence of various parameters.

ACKNOWLEDGMENTS

We thank S. H. Lee, S. Ishihara, and T. Arima for fruitful discussions. The present work was partly supported by a Grant-In-Aid for Scientific Research from Ministry of Education, Culture, Sports, Science and Technology, Japan. The synchrotron power experiments were performed at the SPring-8 BL02B2 with approval of the Japan Synchrotron Radiation Research Institute (JASRI).

*Present address: Department of Physics, Waseda University, Tokyo 169-8555, Japan.

[1] H. L. Yakel and W. C. Koehler, Acta Crystallogr. **16**, 957 (1963).
[2] I. G. Ismailzade and S. A. Kizhaev, Fizika Tverdogo Tela, **7**, 298 (1965) [Sov. Phys. Solid State **7**, 236 (1965)].
[3] K. Lukaszewicz and J. Karut-Kalicinska, Ferroelectrics **7**, 81 (1974).
[4] E. F. Bertaut and M. Mercier, Phys. Lett. **5**, 27 (1963).
[5] W. C. Koehler, H. L. Yakel, E. O. Wollan, and J. W. Cable, Phys. Lett. **9**, 93 (1964).
[6] M. Bieringer and J. E. Greedan, J. Solid State Chem. **143**, 132 (1999).
[7] A. Muñoz, J. A. Alonso, M. J. Martínez-Lope, M. T. Casáis, J. L. Martínez, and M. T. Fernández-Díaz, Phys. Rev. B **62**, 9498 (2000).
[8] T. Katsufuji, S. Mori, M. Masaki, Y. Moritomo, N. Yamamoto, and H. Takagi, Phys. Rev. B **64**, 104419 (2001).
[9] Z. J. Huang, Y. Cao, Y. Sun, Y. Y. Xue, and C. W. Chu, Phys. Rev. B **56**, 2623 (1997).
[10] N. Iwata and K. Kohn, J. Phys. Soc. Jpn. **67**, 3318 (1998).
[11] A. J. Millis, Nature (London) **392**, 147 (1998), and references therein.
[12] C. Moure, M. Villegas, J. F. Fenandez, J. Tartaj, and P. Duban, J. Mater. Sci. **34**, 2565 (1999).
[13] B. B. van Aken, J. W. G. Bos, R. A. de Groot, and T. T. M. Palstra, Phys. Rev. B **63**, 125127 (2001).
[14] I. H. Ismailzade, G. A. Smolenskii, V. I. Nesterenko, and F. A. Agaev, Phys. Status Solidi A **5**, 83 (1971).
[15] M. Takata, E. Nishibori, K. Kato, M. Sakata, and Y. Moritomo, J. Phys. Soc. Jpn. **68**, 2190 (1999).
[16] K. Ohoyama, T. Kanouchi, K. Nemoto, M. Ohashi, T. Kajitani, and Y. Yamaguchi, Jpn. J. Appl. Phys., Part 1 **37**, 3319 (1998).
[17] We note that new small peaks appear at 10° and 16°–17° above 950 K in x-ray diffraction patterns. These peaks do not disappear even after cooling the sample to room temperature, indicating that these are caused by decomposition products.
[18] In the estimation of the magnetic moment, we ignored the trimerization of Mn ions.
[19] T. Katsufuji *et al.* (unpublished).
[20] The existence of small amounts of impurity phases prevents us from precisely determining the Mn valence by simple methods, such as thermogravimetric analysis and titration technique.
[21] M. Fiebig, D. Fröhlich, K. Kohn, St. Leute, Th. Lottermorser, V. V. Pavlov, and R. V. Pisarev, Phys. Rev. Lett. **84**, 5620 (2000).
[22] However, the spin-reorientation transition at low temperatures that Fiebig *et al.* had observed for $LuMnO_3$ (Ref. 21), which should result in the appearance of the (100) peak in neutron scattering, has not been observed in our experiment.
[23] P. Schiffer and A. P. Ramirez, Comments Condens. Matter Phys. **18**, 21 (1996), and references therein.
[24] S.-H. Lee, C. Broholm T. H. Kim, W. Ratcliff II, and S-W. Cheong, Phys. Rev. Lett. **84**, 3718 (2000).
[25] Though its intensity is very weak, a new peak at 20° is seen in the neutron diffraction pattern of $Lu_{0.8}Zr_{0.2}MnO_3$ at 10 K, which indicates the change of the spin orientation with Zr doping and the appearance of the (100) peak as a result.
[26] J. B. Goodenough, *Magnetism and the Chemical Bond* (Wiley, New York, 1963).
[27] D. Fröhlich, St. Leute, V. V. Pavlov, and R. V. Pisarev, Phys. Rev. Lett. **81**, 3239 (1998).
[28] D. I. Khomskii, Bull. Am. Phys. Soc. **46**, C21.002 (2001).